

## **Methods**

### **Mice**

All animal experiments were in accordance with German guidelines and were approved by the relevant local authorities in Essen and Bonn. For the experiments female mice with an age of 7-14 weeks were used unless stated otherwise.

### **NTN induction**

Nephrotoxic sheep serum was generated by immunizing a sheep with homogenized murine renal cortex in CFA, followed by monthly boosting doses in IFA. cGN in mice was induced by i.p. injection of 0.35 ml nephrotoxic serum per mouse, as previously described<sup>1,2</sup>

### **Neutrophil recruitment into the lung**

For recruiting tdTomato<sup>+</sup> neutrophils into the lung a pulmonary mold infection was induced in Catchup<sup>IVM-red</sup><sup>3</sup> mice by intratracheally applying 5 x 10<sup>6</sup> resting *Aspergillus fumigatus* spores (strain ATCC 46645), suspended in 100 µl sterile tap water as previously described<sup>3</sup>. Animals were killed 3h after infection via CO<sub>2</sub> and prepared as described below.

### **Antibody staining and sample preparation**

8 to 12 weeks old female mice (CD11c-EYFP<sup>4</sup>, CX3CR1-EGFP<sup>5</sup>, Catchup<sup>IVM-red</sup><sup>3</sup>) were injected i.v. with 10 µg per mouse CD31-AF647 (Biolegend, Cat# 102516) in PBS (total volume 150 µl) and sacrificed by CO<sub>2</sub> 10 min after injection.

Immediately after killing mice were transcardially perfused with 15 ml of cold PBS/5 mM EDTA and perfusion-fixed with 15 ml of cold 4% PFA/PBS, pH = 7.4. After perfusion organs were removed and post-fixed in cold 4% PFA/PBS pH = 7.4 at 4-8 °C considering organ-specific incubation times (**Supplementary table 2**).

### **Sample dehydration and Clearing**

After perfusion and post-fixation with 4% PFA/PBS samples were dehydrated with Ethanol (EtOH), pH = 9.0 thereby considering organ-specific concentrations and incubation times (**Supplementary table 2**).

Incubation of all samples was performed at 4-8 °C in gently shaking 5 ml tubes. For optimal tissue dehydration the incubation with 100% EtOH had to be done twice to remove all left over water molecules.

As mineralized compact bones slowed down the dehydration process, longer incubation times of 12 h per concentration EtOH were required.

After dehydration the samples were transferred to Ethyl cinnamate (Sigma Aldrich, Cat# 112372) and incubated while gently shaking at room temperature RT (the freezing/melting point of Ethyl cinnamate is 6-8 °C) until they became transparent.

For comparison of our new clearing reagent with other established “solvent based” clearing protocols tissue clearing was performed as described<sup>6-9</sup> with slight modifications.

The solvent based clearing via Di-Benzylether (DBE, Sigma Aldrich, Cat# 33630) of Erturk et al. (2012) was performed with modifications based on our EtOH-ECi clearing protocol. As Tetrahydrofuran might form explosive peroxides in contact with air, we exchanged the dehydration agent to Ethanol. The used Ethanol-concentrations and incubation times were equal to our EtOH-ECi protocol. After dehydration the organs were transferred to DBE and incubated at room temperature until they became transparent.

According to Schwarz et al. (2015), Becker et al. (2008) and Acar et al. (2015) organs were dehydrated in graded Ethanol or tert-Butanol series of 30 %, 50 %, 70 %, 80 %, 96 % and twice 100 % (vol./vol.) for 24 h each with adjusted pH = 9.0 at RT or 30 °C in gently shaking 5 ml tubes. The following tissue clearing was performed via Benzyl alcohol-Benzyl benzoate (BABB; Benzyl alcohol, Sigma Aldrich, Cat# 402834; Benzyl benzoate, Sigma Aldrich, Cat# B6630).

As an example for a water based “simple immersion” tissue clearing the protocol of SeeDB clearing was performed<sup>10</sup>. Here the samples were dehydrated via increasing fructose-solution series of 20 %, 40 %, 60 % (wt./vol.) for 8 h at RT and 80 % and 100 % (wt./vol.) with 0.5 % α-Thioglycerol for 12 h at RT. The final clearing step was based on 24 h incubation at RT with SeeDB (80.2 % (wt/wt) fructose) in gently shaking 5 ml tubes.

### **Light-Sheet Fluorescence Microscopy (LSFM)**

To image whole organs a LaVisionBioTec (Bielefeld, Germany) UltraMicroscope with an Olympus MVX10 zoom microscope body, an LVBT Laser module, an Andor Neo sCMOS camera with a pixel size of 6.5 x 6.5 μm<sup>2</sup> and detection optics with an optical magnification range of 1.26 x - 12.6 x and an NA of 0.5 was used.

For EYFP and EGFP excitation a 488 nm Optically Pumped Semiconductor Laser (OPSL), for tdTomato excitation a 561 nm OPSL and for CD31-AF647 excitation a 647 nm Diode Laser was used. Emitted wavelengths were detected with specific detection filters: 525/50 nm for EGFP, 545/30 nm for EYFP, 595/40 nm for tdTomato and 680/30 nm for CD31-AF647. As the excitation optics of the microscope provided a

light sheet thickness of 5 - 40  $\mu\text{m}$  the Z-step size was set to 5  $\mu\text{m}$  for all measurements. The optical zoom factor varied from 1.6 x – 10 x.

### **Single and two-photon laser scanning microscopy (LSM)**

For high magnification imaging of the samples a Leica TCS SP8 fully automated epifluorescence confocal microscope with AOTF and AOBS scanoptics, HyD detection, 2-Photon (MP) and compact OPO on a DM6000 CFS frame was used (Leica, Mannheim, Germany).

Imaging of glomeruli in cleared kidneys was performed via a 25 x HCX IRAPO L objective with an NA of 0.95 in water. Fluorescent signals were generated via sequential scans, exciting CD31-AF647 via single photon excitation using a HeNE laser at 633 nm and detecting in confocal mode with an internal HyD at 660-720 nm. The second sequence was performed with a 2-Photon laser tuned to 960 nm for SHG-detection at 460/50 nm and autofluorescence detection at 520/50 nm, both detected with external PMTs NDD1 and NDD2.

### **Image reconstruction**

For image analysis ImageJ (Image Processing and Analysis in Java, <http://imagej.nih.gov/ij/>) and IMARIS 8.1.2 (Bitplane, Switzerland) were used. 3-D rendering of LSFM data as well as LSM data was performed via IMARIS software (final movies were put together and labeled using Microsoft Movie Maker). Supplementary movies were strongly downsampled to accommodate the extremely large original data sets (typically multi gigabytes). The loss of optical image quality in the final supplementary movies was kept at a minimum, however impossible to be avoided completely.

### **Statistics**

Statistical analysis of qWOB kidney data was performed with GraphPad Prism 6 software (GraphPad Inc., California, USA). Depending on the type of data two-tailed, unpaired t-tests or chi-square test were used as indicated in the legend of Fig. 3<sup>11</sup>.

### **Fluorescence stability**

For quantification of long time fluorescence stability, DBE or ECi cleared CD11c-EYFP kidneys were measured repetitively over one month with constant settings via the Ultramicroscope. The generated raw data were imported as an image sequence into ImageJ. The mean intensity within a defined region of interest (ROI), which corresponded to the size of CD11c-EYFP positive cells, was measured over all Z-slices at 100 different positions for fluorescent cells and at 100 autofluorescent positions within

the kidney tissue. To equalize small intensity variations caused by signal loosening in deep tissue or by oscillations in laser intensity at different measurement time points the signal height was calculated as a fluorescence/autofluorescence ratio ( $y$ ), based on the intensity means of the 100 arbitrary fluorescent cell bodies and autofluorescent tissue areas per Z-stack. Regarding the ratio calculation the errors of intensity-means were taken into consideration by calculating the error propagation<sup>6</sup> according to the following formula:

$$\frac{\delta y}{y} = \sqrt{\left(\frac{\delta x_1}{x_1}\right)^2 + \left(\frac{\delta x_2}{x_2}\right)^2}$$

Here  $x_1$  denotes the mean-intensity of EYFP positive cells and  $\delta x_1$  the error of  $x_1$ , while  $x_2$  describes the error of autofluorescence intensity and  $\delta x_2$  the error of  $x_2$ .

### **Tissue shrinkage**

For analyzing the effect of sample dehydration and clearing on tissue shrinkage different dehydration agents and clearing agents were compared. After antibody injection (10 µg CD31-AF647 i.v.) and sacrificing mice via CO<sub>2</sub> one kidney was disconnected from blood circulation by clipping the afferent vessels. The mice were perfused as described above. After perfusion fixation both kidneys were removed, leading to one fixed and one un-fixed sample per mouse. Both kidneys were imaged via LSFM for analyzing the effect of 4% PFA/PBS fixation on tissue shrinkage via “segmentation of kidney region”. After imaging both kidneys were post-fixed whereat the so far un-fixed kidney was incubated longer in 4 % PFA/PBS for at least 5 h at 4-8 °C. Both kidneys were then cleared via either Ethanol-ECi, Ethanol-DBE or tert-Butanol-BABB as described above. All cleared organs were imaged via LSFM for clarifying the effect of different clearing protocols on tissue shrinkage via “segmentation of kidney region” analysis.

### **Clearing efficiency**

The clearing efficiency of different clearing procedures was compared via spectrophotometric analysis.

Here the protocols of tert-Butanol-BABB, EtOH-DBE, EtOH-ECi and SeeDB clearing were performed as described above. The clearing efficiency was analyzed on C57BL/6 lungs, as an example for soft tissues, and tibiae, as an example for hard tissues.

For spectrophotometric measurements a Thermo Scientific™ NanoDrop 2000c UV-Vis Spectrophotometer was used. The Tissue absorption was detected over a spectral range from 400 nm to 740 nm with 20 nm steps covering the excitation and detection range of the LaVisionBioTec (Bielefeld, Germany) UltraMicroscope.

## Image analysis

In order to evaluate the kidney volume as well as the number, diameter and volume of glomeruli we developed an automated analysis procedure of light sheet fluorescence microscopy data. The image analysis algorithm was implemented in the programming language “python” (<https://www.python.org/>) and was carried out fully automatically. The procedure includes (1) preprocessing of image data, (2) segmentation of the kidney region, (3) segmentation of the glomeruli, and (4) quantification of the segmented regions. The first three steps were performed for each layer of the image z-stacks separately to reduce computational load, while the quantification was carried out after combining segmentation results from all layers.

### Preprocessing of image data

Each z-layer was processed with a median filter of radius 3 pixels to reduce the noise level. Then, the z-layer was normalized such that its maximum intensity value  $N(x, y)$  equals 255, corresponding to an 8-bit image:

$$N(x, y) = \frac{I(x, y)}{\max\{I(x, y)\}} \cdot 255$$

Here,  $I(x, y)$  denotes a z-layer of an image after the median filtering and  $\max\{I(x, y)\}$  corresponds to the maximum value of the median-filtered layer.

### Segmentation of the kidney region

In order to detect the kidney region  $K(x, y)$ , the following sequence of steps was performed for each normalized z-layer  $N(x, y)$ :

1. The size of  $N(x, y)$  was reduced by the factor of 10 by means of a linear interpolation, resulting into the z-layer  $N'(x, y)$ . This was done to reduce the computational load and smooth intensity variations.
2.  $N'(x, y)$  was processed with a Gaussian filter of width  $\sigma = \frac{3 \mu m}{s_{xy}}$ , where  $s_{xy}$  denotes the voxel size in the x-y-plane, yielding the z-layer  $S(x, y)$ .
3. The 40-th percentile of  $S(x, y)$  was computed and designated as  $p_{40}$ . This value was chosen to represent a typical intensity of the background, because the kidney tissue in the samples did not occupy more than 60% of the image area.
4.  $S(x, y)$  was thresholded at  $2 \cdot p_{40}$ , which was empirically determined to be the optimal threshold:

$$T(x, y) = \begin{cases} 1, & \text{if } S(x, y) > 2 \cdot p_{40} \\ 0, & \text{if } S(x, y) \leq 2 \cdot p_{40} \end{cases}.$$

After thresholding, some dark areas inside the kidney were classified as background (**Supplementary Fig. 6a**), which normally can be corrected by the procedure of closing

holes. This, however, fails if these regions are connected to the background, as for the case shown in **Supplementary Fig. 6**. To overcome this problem, the following three steps were performed.

5. In order to close the connection of dark regions inside the kidney and the background, morphological dilation of  $T(x, y)$  was performed with a disk of radius 5 pixels, resulting into the z-layer  $D(x, y)$  (**see supplementary Fig. 6b**).
6. Holes in  $D(x, y)$  were closed. To this end, we first identified the regions that belong to the background (*i.e.*, that have a value of 0), but were not connected to the background; these regions were labeled as the foreground (*i.e.*, assigned the value 1). The result was designated as  $F(x, y)$  (**see supplementary Fig. 6c**).
7. Morphological erosion of  $F(x, y)$  was performed with a disk of radius 5 pixels to return the binary kidney mask to its normal size (*i.e.* the size before step 5). The result was designated as  $E(x, y)$  (**see supplementary Fig. 6d**).
8. Connected foreground regions in  $E(x, y)$  were detected (von Neumann neighborhood) and each of them was assigned with a unique label  $l \in [1; n]$ , where  $n$  was the total number of connected regions in the current z-layer. The result was stored in  $L(x, y)$ .
9. After steps 1 to 8, some areas of background with slightly higher intensity were still classified as foreground regions (**see supplementary Fig. 6a-d, upper-right corner**). To handle these artefacts, mean intensity values of  $S(x, y)$  were computed for each connected region:

$$m(l) = \text{mean}\{S(x'(l), y'(l))\}, \text{ where } x'(l), y'(l) \text{ correspond to the pixels where } L(x, y) = l$$

10. Regions with low mean intensity values were removed (**see supplementary Fig. 6e**):

$$K'(x, y) = \begin{cases} 1, & \text{if } L(x, y) \text{ in } l', \\ 0, & \text{otherwise} \end{cases}, \text{ where } l' \text{ were the labels with } m(l') \geq 2 \cdot$$

$p_{40}$

11. The size of the kidney mask  $K'(x, y)$  was restored to normal size, *i.e.* increased by the factor of 10, by means of linear interpolation. The resulting binary kidney mask was designated as  $K(x, y)$ .

After the segmentation of each z-layer, all layers  $K(x, y)$  were combined into a three-dimensional array, which was designated as  $K(x, y, z)$ .

### Segmentation of the glomeruli

Due to uneven intensity of kidney tissue in some images (**see, e.g., supplementary Fig. 7a**), simple thresholding did not give adequate results (**see supplementary Fig. 7b**). In

order to detect the glomeruli regions  $G(x, y, z)$  in the kidney background with varying intensity, the following sequence of steps was performed for each normalized z-layer  $N(x, y)$ :

1. Morphological opening (erosion + dilation) of  $N(x, y)$  was performed with a disk of radius  $r = \frac{r_{max}}{s_{xy}}$ , where  $r_{max}$  corresponds to the maximally allowed radius of glomeruli and equals to  $65 \mu m$ . This resulted in  $O(x, y)$  (**see supplementary Fig. 7c**), where all objects of size less than  $r_{max}$  were removed.
2. The morphologically opened image was subtracted from the initial image, with resulted in the correction of the uneven background (**see supplementary Fig. 7d**):

$$C(x, y) = N(x, y) - O(x, y)$$

In the resulting image only objects with size less than  $r_{max}$  were conserved.

3.  $C(x, y)$  was normalized such that its values were between 0 and 255:

$$\begin{aligned} C'(x, y) &= C(x, y) - \min\{C(x, y)\}, \\ C''(x, y) &= \frac{C'(x, y)}{\max\{C'(x, y)\}} \cdot 255 \end{aligned}$$

4. The 75-th percentile  $p_{75}$  of  $C''(x', y')$  was computed to represent a typical intensity of the kidney tissue, where  $x', y'$  refer to the pixels where  $K(x, y) = 1$ .
5. Otsu's threshold  $t$  of the image  $C''(x, y)$  was computed. For pixels with  $t > p_{75} \cdot 1.5$  Otsu-thresholding was performed:

$$G(x, y) = \begin{cases} 1, & \text{if } C''(x, y) > t \\ 0, & \text{otherwise} \end{cases}$$

If  $t \leq p_{75} \cdot 1.5$  then  $G(x, y) = 0$ . This situation represented outer z-layers where no glomeruli were present.

6. Morphological opening (erosion + dilation) of  $G(x, y)$  was performed with a disk of radius  $r = 0.5 \cdot \frac{r_{min}}{s_{xy}}$ , where  $r_{min}$  corresponds to the minimal allowed radius of glomeruli and equals to  $15 \mu m$ . In the output binary image  $G'(x, y)$  only objects with a radius more than  $0.5 \cdot r_{min}$  remained (**see supplementary Fig. 7e**).

After the segmentation of each z-layer, all layers  $G'(x, y)$  were combined into a three-dimensional array, and regions connected in 3D were assigned with a unique label. The result was designated as  $G(x, y, z)$ .

### Quantification of the segmented regions

The kidney volume  $V_K$  was evaluated from the kidney mask  $K(x, y, z)$  of each corresponding z-stack:

$$V_K = P_K \cdot s_{xy}^2 \cdot s_z,$$

where  $P_K$  is the number of pixels corresponding to the kidney region, and  $s_{xy}$  and  $s_z$  denote the voxel size in xy and z, respectively.

The volume of each individual glomerulus was computed analogously from the labeled glomeruli image  $G(x, y, z)$ :

$$V_{G_l} = P_{G_l} \cdot s_{xy}^2 \cdot s_z, \quad l \in [1, n],$$

where  $P_{G_l}$  is the number of pixels corresponding to the  $l$ -th label in  $G(x, y, z)$ ,  $n$  is the total number of labeled region.

In order to exclude object with inadequate size from further computations, the minimum and maximum allowed volumes were computed as follows:

$$V_{max} = \frac{3}{4} \cdot \pi \cdot r_{max}^3 \quad \text{and} \quad V_{min} = \frac{3}{4} \cdot \pi \cdot r_{min}^3,$$

where  $r_{min}$  and  $r_{max}$  correspond to minimally and maximally allowed radii of glomeruli, which were assumed to be equal to 15 and 65  $\mu\text{m}$ , respectively.

The following condition was controlled for the  $V_{G_l}$  of each labeled region:

$$V_{min} \leq V_{G_l} \leq V_{max}.$$

If the condition was satisfied, the volume and the coordinates of the center of mass of the corresponding region were stored for the further analysis. The number of glomeruli in a kidney was evaluated as the number of labeled regions satisfying the above volume restriction.

### Comparison of kidney volumes

The comparison of kidney volumes before fixation, after fixation and after clearing was done by automated image analysis. Because of a low image contrast in non-cleared samples, the procedure for segmentation of kidney regions had to be adapted accordingly. The following sequence of steps was applied for each separate z-layer:

1. Median filtering, radius 3 pixels
2. Histogram equalization: normalizing the image to the 5-th percentile from below and to the 99-th percentile from above
3. Gaussian filtering of the equalized image,  $\sigma = \frac{30 \mu\text{m}}{s_{xy}}$ , where  $s_{xy}$  denotes the voxel size in the x-y-plane
4. Otsu thresholding of the Gaussian-filtered image

5. Reducing the size of the thresholded image by the factor of 10 by means of a linear interpolation. This was done to reduce the computational load for the further morphological operations.
6. Morphological closing of the downsized image with a disk of radius  $r = \frac{300 \mu m}{s_{xy}}$ .  
This was done to fuse the foreground fragments into one kidney region, which was – in some cases – detected as several pieces due to irregular illumination pattern in non-cleared samples.
7. Closing holes in the segmented kidney region
8. Restoring the kidney mask to normal size
9. Computing the ratio of median intensities in the foreground and in the background. If this ratio was less than 3, the layer was excluded from the volume computation due to the absence of the object of interest (kidney region).

### **Computing time**

The computations were carried out on a GNU/Linux server (SUSE), Intel® Xeon ® CPU E7-4890 v2 @ 2.80GHz x 60, 757 GB RAM. The average computing time for one Z-stack was  $2.8 \pm 0.7$  hours. The computations were carried out fully automatically and the algorithm could be easily adjusted to run on computers with lower RAM and CPU resources.

## References:

- 1 Hochheiser, K. *et al.* Kidney Dendritic Cells Become Pathogenic during Crescentic Glomerulonephritis with Proteinuria. *J Am Soc. Nephrol* **22**, 306-316 (2011).
- 2 Scholz, J. *et al.* Renal dendritic cells stimulate IL-10 production and attenuate nephrotoxic nephritis. *J Am Soc. Nephrol* **19**, 527-537 (2008).
- 3 Hasenberg, A. *et al.* Catchup: a mouse model for imaging-based tracking and modulation of neutrophil granulocytes. *Nat Methods* **12**, 445-452 (2015).
- 4 Lindquist, R. L. *et al.* Visualizing dendritic cell networks in vivo. *Nat Immunol* **5**, 1243-1250 (2004).
- 5 Jung, S. *et al.* Analysis of fractalkine receptor CX(3)CR1 function by targeted deletion and green fluorescent protein reporter gene insertion. *Mol Cell Biol* **20**, 4106-4114 (2000).
- 6 Schwarz, M. K. *et al.* Fluorescent-protein stabilization and high-resolution imaging of cleared, intact mouse brains. *PLoS one* **10**, e0124650 (2015).
- 7 Becker, K., Jahrling, N., Saghafi, S., Weiler, R. & Dodt, H. U. Chemical clearing and dehydration of GFP expressing mouse brains. *PLoS one* **7**, e33916 (2012).
- 8 Acar, M. *et al.* Deep imaging of bone marrow shows non-dividing stem cells are mainly perisinusoidal. *Nature* **526**, 126-130 (2015).
- 9 Erturk, A. *et al.* Three-dimensional imaging of solvent-cleared organs using 3DISCO. *Nat Protoc* **7**, 1983-1995 (2012).
- 10 Ke, M. T., Fujimoto, S. & Imai, T. SeeDB: a simple and morphology-preserving optical clearing agent for neuronal circuit reconstruction. *Nat Neurosci* **16**, 1154-1161 (2013).
- 11 Bohm, G. & Zech, G. *Introduction to Statistics and Data Analysis for Physicists*. (Verlag Deutsches Elektronen-Synchrotron, 2010).

## **Supplementary figures**

### **Supplementary figure 1: Preservation of multiple FPs after ECi clearing**

ECi clearing preserves multiple fluorescent proteins (FPs) as EGFP (green), EYFP (yellow) and tdTomato (red). GFP preservation is shown via clearing of a CX3CR-EGFP mouse brain and EYFP preservation via fluorescence positive cells in the cleared kidney of a CD11c-EYFP mouse. The pulmonary *Aspergillus fumigatus* infection of a Catchup<sup>IVM-red</sup> mouse recruited tdTomato<sup>+</sup> neutrophils into the lung, which were detected after ECi clearing. Scalebars = 50 µm

### **Supplementary figure 2: ECi clearing of CD11c-EYFP calvaria**

(A) Overview of a whole calvaria showing the paired frontal bones (F), the paired parietal bones (P) and the interparietal bone (IP) via autofluorescence signal (grey). The entire vascularization of the calvaria is visualized via specific vessels staining (CD31, red), including big vessels along the sagittal suture (filled white arrowheads) and the coronal suture (empty white arrowheads) as well as the sinusoidal network of the bone marrow (white stars). Scalebar = 1000 µm. (B) Increased magnification of white box (A) shows CD11c-EYFP positive cells (yellow) attached to the sinusoidal bone marrow vascularization (red) inside the calvarial bone (grey). Scalebar = 100 µm

### **Supplementary figure 3: ECi Clearing of a mouse heart**

(A) Imaris 3D-reconstruction of Light sheet microscopy data showing the muscle structure (autofluorescence, grey) and vascularization (CD31, red) of an ECi cleared mouse heart. (B) Optical “clipping” of the 3D-reconstruction opens the right ventricle of the heart, showing the vessel structures of the ventricle wall as well as the chordae tendinae (white arrow) and the papillary muscles (white arrowheads) inside the ventricle. In the background, the interventricular septum is shown. Scalebars = 1000 µm

### **Supplementary figure 4: ECi clearing of murine long bones**

(a) 3D-reconstruction of distal, intermediate and proximal phalanges of a mouse hind paw based on autofluorescence (grey) and vessel staining (CD31, red). (b) Optical “clipping” of the 3D-model opens the bone and provides an insight view into the bone structure, showing the periosteum (white arrow), the compact bone (white clip), the endosteum (empty white arrowhead), the bone marrow (white star) and its vascularization (filled white arrowhead). Scalebars = 200 µm

### **Supplementary figure 5: Automated quantification of immune cells**

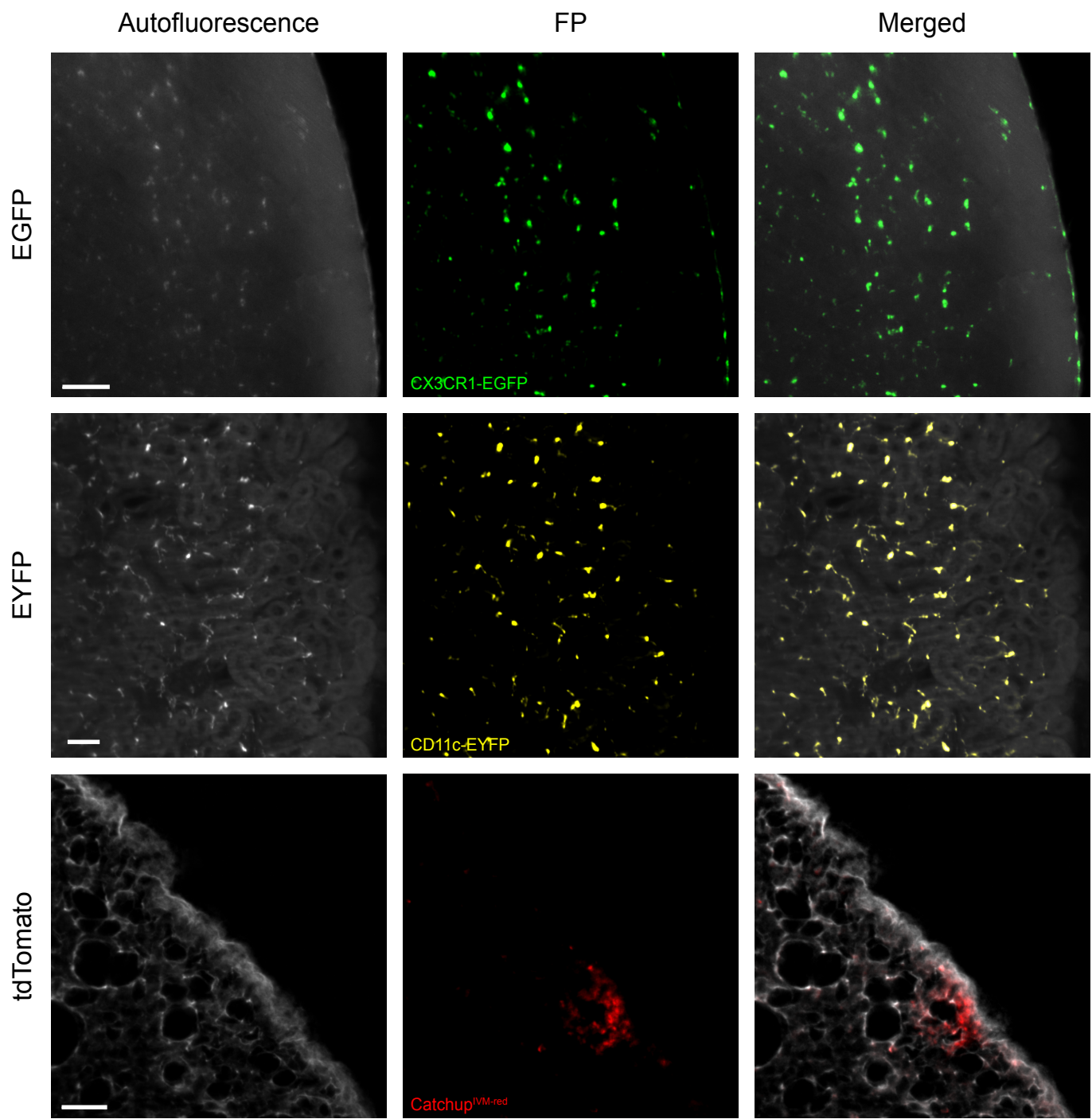
CD11c-eYFP positive cells (yellow) in the confocal stack of Figure 2C are visualized via the Blend (A) and the maximum intensity projection (MIP) rendering algorithms of the IMARIS software (B). (C) Automatically quantified cells are indicated via turquoise dots in the whole z-stack. In this example the number of counted dendritic cells was 5,304.

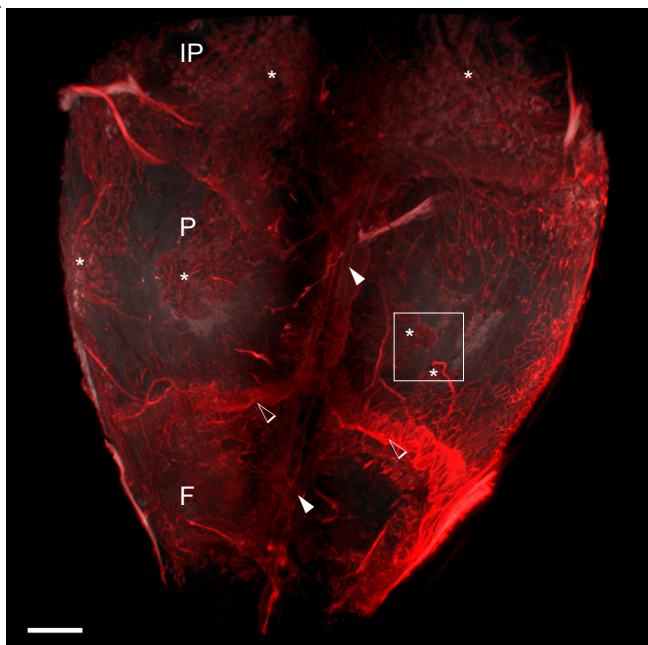
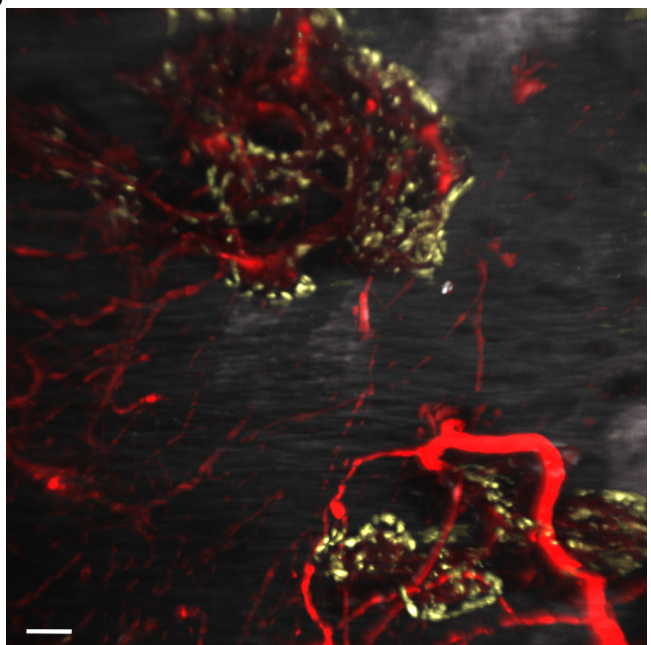
### **Supplementary figure 6: Volume calculation of kidneys**

Segmentation of kidney tissue including closing holes in the kidney binary mask (a-d) and removal of background regions misclassified as foreground (e). (a) Kidney outline after thresholding: some dark areas inside the kidney are classified as background. (b) Kidney outline after morphological dilation of (a): the connection of dark kidney areas with the background is closed. (c) Kidney outline after closing holes in (b). (d) Kidney outline after morphological erosion of (c). (e) Kidney outline after removal of the misclassified background regions (e.g. a-d, upper-right corner).

### **Supplementary Figure 7: Quantification of glomeruli.**

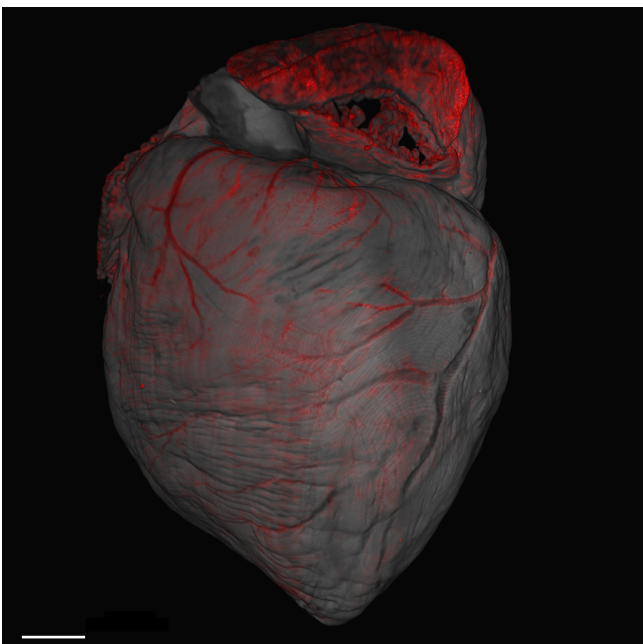
(a) Exemplary z-layer with uneven kidney background. (b) Outlines of glomeruli after thresholding at  $3 \cdot p_{50}$ , where  $p_{50}$  is the median intensity in the kidney region; some glomeruli in dark areas were classified as background, while some background in bright areas was detected as glomeruli. (c) Morphological opening of (a) with a disk of radius  $r = \frac{65 \mu m}{s_{xy}}$ , where  $s_{xy}$  is the voxel size in the x-y plane. (d) The result of subtracting (c) from (a). (e) Outlines of glomeruli after Otsu thresholding of (d) and removal of small objects (see step 6 of glomeruli segmentation in online methods).



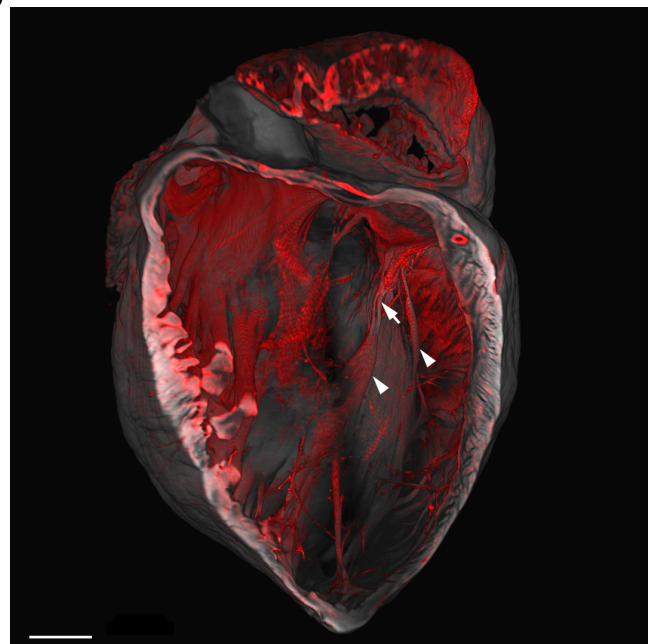
**A****B**

CD31 CD11c-eYFP Autofluorescence

A

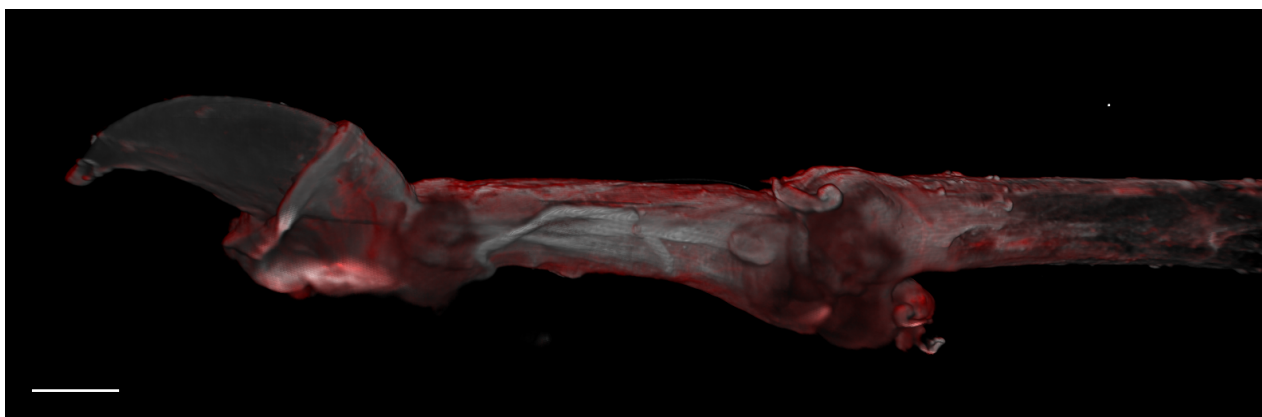


B

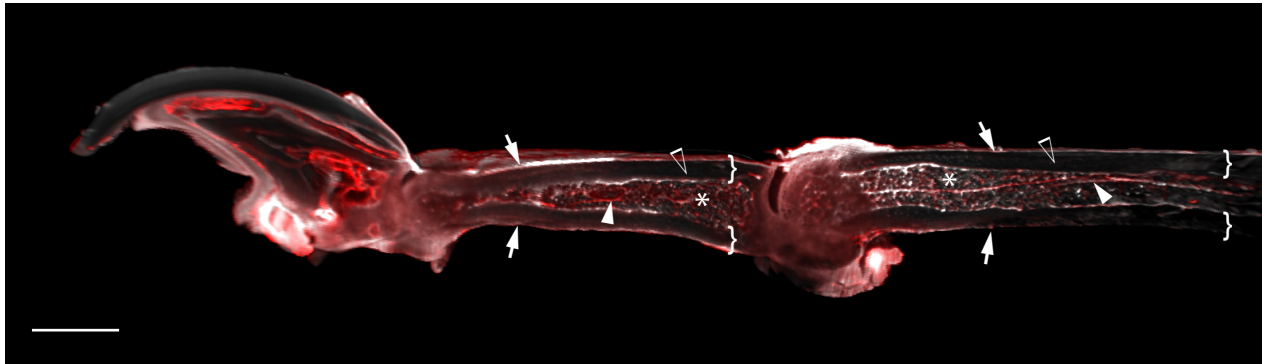


CD31 Autofluorescence

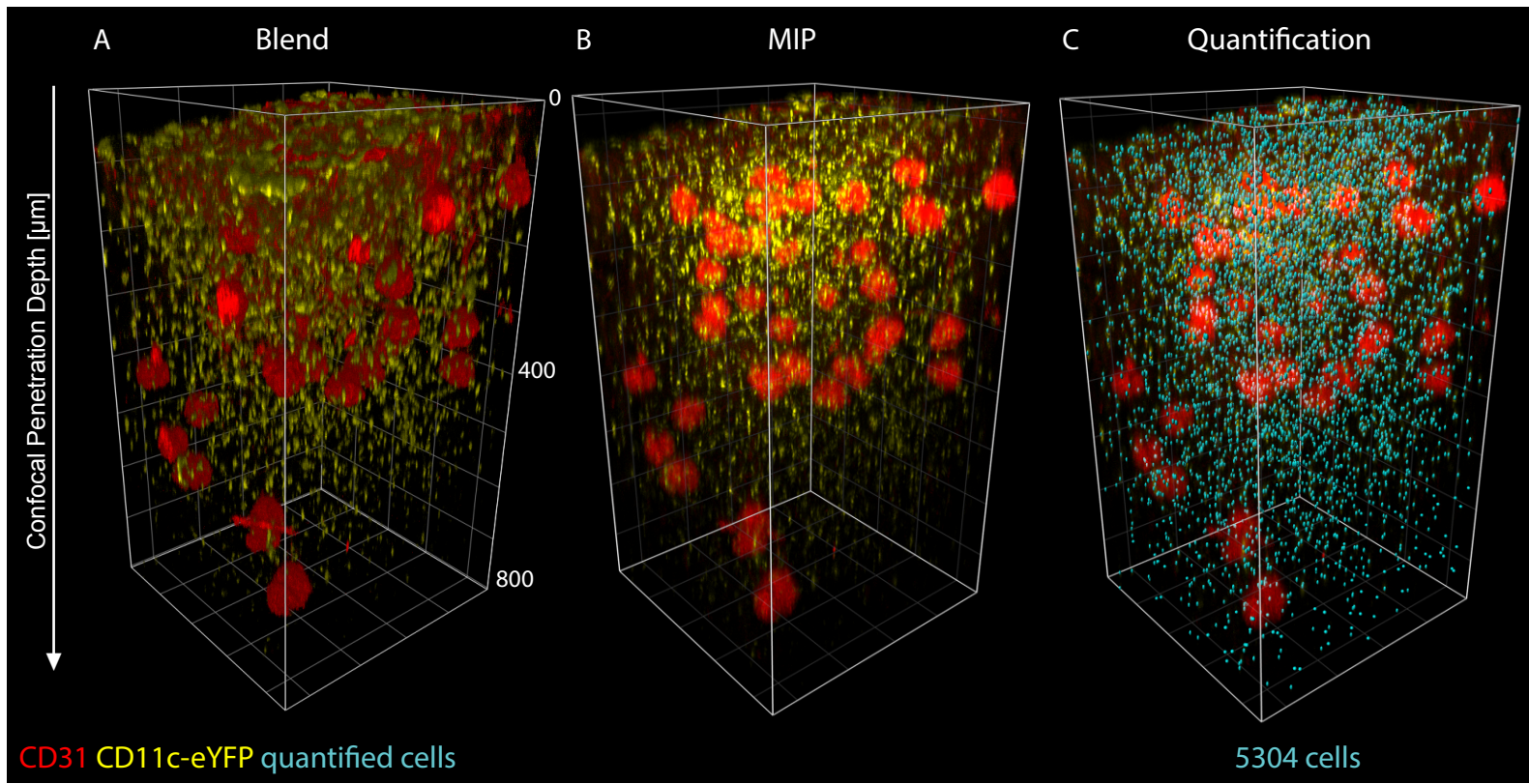
A



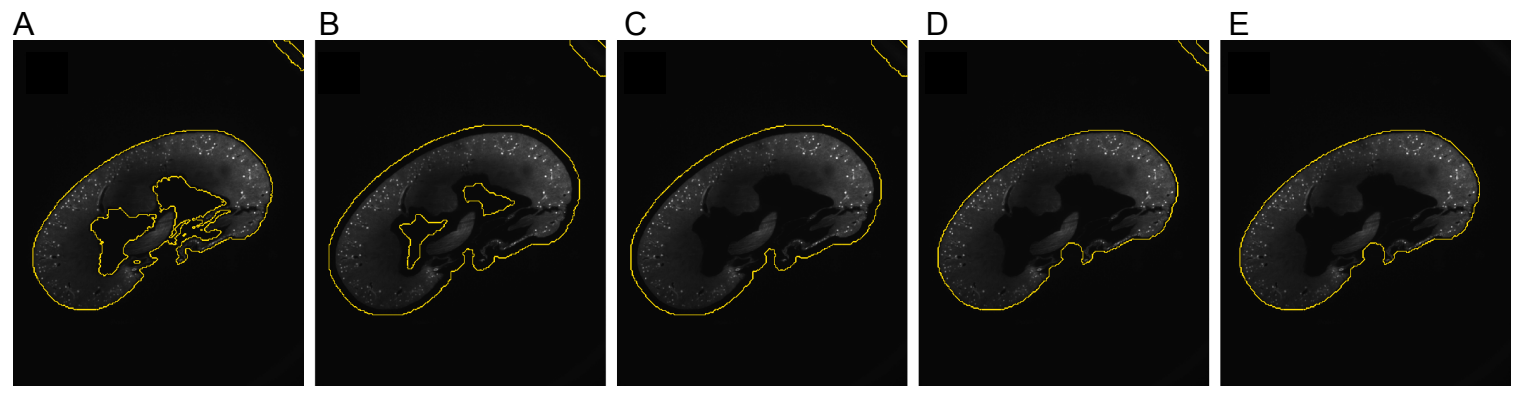
B



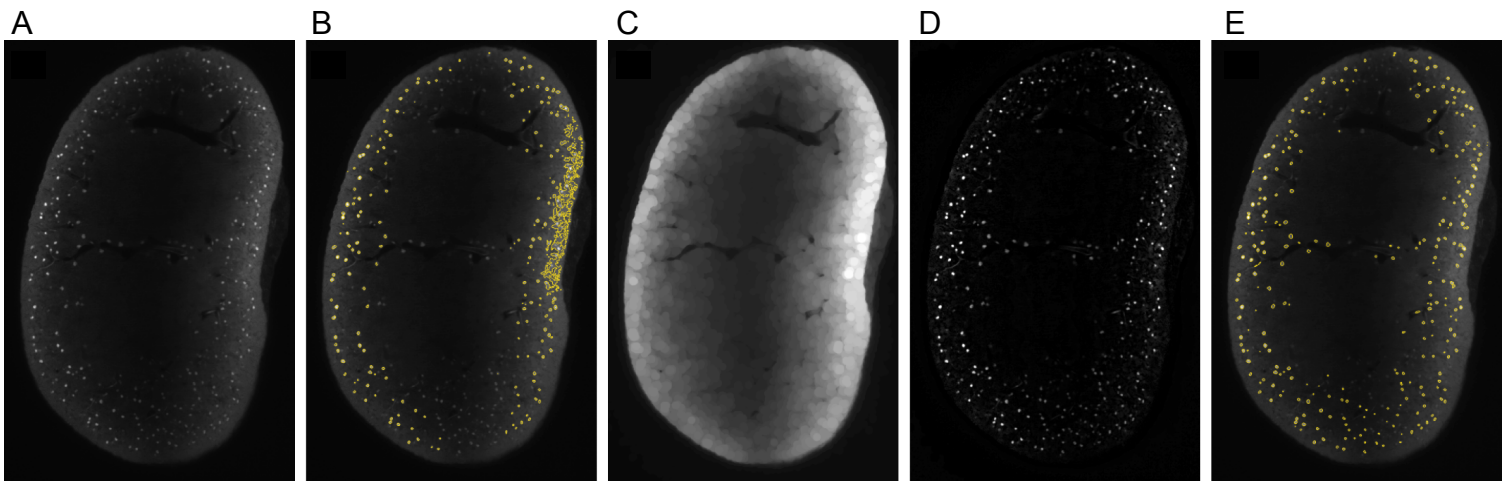
CD31 Autofluorescence



Supplementary Figure 5

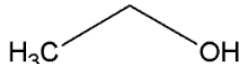
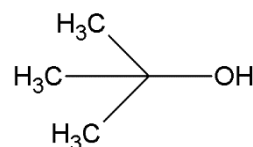
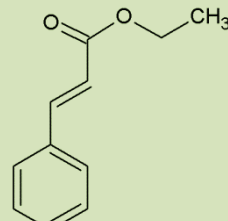
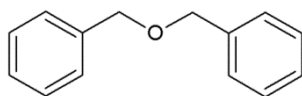


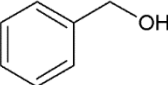
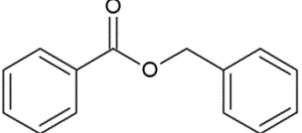
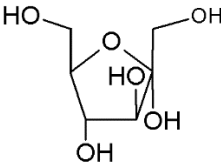
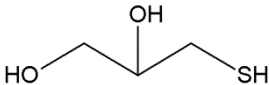
Supplementary Figure 6



Supplementary Figure 7

**Supplementary Table 1: Chemical structures and molecular characteristics of solvent-based clearing agents**

	Structure	Name	Synonym	Properties	Safety Statements
Dehydration Agents		Ethanol		MF = C <sub>2</sub> H <sub>6</sub> O RI (nD20) = 1.360	 <b>WARNING</b> H225-H319 P210-P280-P305 + P351 + P338-P337 + P313-P403 + P235
		Tetrahydrofuran	THF	MF = C <sub>4</sub> H <sub>8</sub> O RI (nD20) = 1.407	 <b>DANGER</b> H225-H319-H335-H351 P210-P261-P281-P305 + P351 + P338 <b>May form explosive peroxides!</b>
		tert-Butanol		MF = C <sub>4</sub> H <sub>10</sub> O RI (nD20) = 1.394	 <b>DANGER</b> H225-H319-H332-H335 P210-P261-P305 + P351 + P338
Clearing Agents		Ethyl Cinnamate <i>ethyl (2E)-3-phenylprop-2-enoate</i>	ECi	MF = C <sub>11</sub> H <sub>12</sub> O RI (nD20) = 1.558	
		Di-Benzylether	DBE	MF = C <sub>14</sub> H <sub>14</sub> O RI (nD20) = 1.561	 <b>WARNING</b> H335-H410 P273-P304 + P340 + P312-P391-P501

		Benzyl Alcohol <i>phenylmethanol</i>	<b>BABB</b>	MF = C <sub>7</sub> H <sub>8</sub> O RI (nD20) = 1.539	 <b>WARNING</b> H302 + H332-H319 P261-P301 + P312 + P330-P304 + P340 + P312-P305 + P351 + P338
		Benzyl Benzoate		MF = C <sub>14</sub> H <sub>12</sub> O <sub>2</sub> RI (nD20) = 1.568	 <b>WARNING</b> H302-H411 P273
		Fructose		MF = C <sub>6</sub> H <sub>12</sub> O <sub>6</sub> RI (nD20) = 1.616	
		1-Thioglycerol	<b>SeeDB</b>	MF = C <sub>3</sub> H <sub>8</sub> O <sub>2</sub> S RI (nD20) = 1.526	 <b>DANGER</b> H302-H311-H315- H319-H335 P261-P280-P305 + P351 + P338-P312

MF = molecular formula

RI = refractive index



Flammable



Harmful



Health Hazard



Environmental  
Hazard



Toxic

Listed codifications of pictograms, hazard statements ("H") and precautionary statements ("P") are in accordance with the UNECE defined Globally Harmonized System of Classification and Labelling of Chemicals (GHS) Rev. 6 (2015) and based on manufacturer's instructions.

**Supplementary Table 2: Organ-specific incubation times for post-fixation, dehydration and optical clearing**

Organ	4% PFA/PBS* pH = 7.4 4-8 °C	30% EtOH pH = 9.0 4-8 °C	50% EtOH pH = 9.0 4-8 °C	70% EtOH pH = 9.0 4-8 °C	2x 100% EtOH 4-8 °C	ECi RT
Calvaria	2 h	-	4 h	4 h	4 h	15 min
Heart	2 h	-	4 h	4 h	4 h	2 h
Kidney	2 h	-	4 h	4 h	4 h	2 h
Bones	4 h	-	12 h	12 h	12 h	6 h

\* incubation times additionally to 4% PFA/PBS-perfusion (pH=7.4)

**Supplementary Table 3: Total data generation time and Hands-on time per kidney**

Procedure		Total Time [min]	Hands-on Time [min]
<b>Antibody staining</b>	i.v. Injection	25	5
<b>Sample preparation</b>	organremoval	5	5
	perfusion	10	10
	Post-fixation in 4 % PFA/PBS	120	1
	Dehydration 50 % EtOH	240	1
	Dehydration 70 % EtOH	240	1
	Dehydration 100 % EtOH	240	1
	Dehydration 100 % EtOH	240	1
	ECi clearing	120	1
<b>Microscopy</b>	LSFM	45	15
<b>Data analysis</b>	Fully automated	168	5
<b>Total [min]</b>		<b>1,453</b>	<b>46</b>
<b>Total [h]</b>		<b>24.17</b>	<b>0.77</b>

## **Supplemental videos**

### **Supplementary video 1: Calvaria**

ECi-cleared calvarial bone is visualized via its autofluorescence signal (grey). Additionally the entire blood vessel system is labeled and imaged via specific endothelial antibody staining (CD31, red).

### **Supplementary video 2: Heart**

3D-reconstruction of an ECi cleared liver heart. Autofluorescence of the heart muscle tissue (grey) offers detailed structural information about the external and internal organ structure. The vasculature of the heart was specifically stained via CD31 (red). Clipping of the 3D model allows a view inside the right ventricle showing its intracardial papillary muscles and chordae tendinae as well as the ventricular septum.

### **Supplementary video 3: Whole organ imaging of healthy and NTN kidneys**

3D-reconstruction of ECi cleared kidneys. The surface and the complex vascular organization (CD31, red) of an entire kidney is shown via optical clipping into the kidney volume. The renal, medullary and cortical vessels appear tube like whereas the small glomerular capillaries have a globular shape. Higher zoom factor of the lightsheet microscope allows a more detailed visualization of the glomeruli.

Laser scanning confocal and 2-photon (dat wüsste ich aber, dat dat Elmi ist!!!) microscopy allows an even higher magnification of the glomeruli. The glomerular capillaries (CD31, red) are normally shaped in kidneys of untreated mice, filling the majority of the Bowman's capsule volume (SHG, blue). The surrounding kidney tubules are visualized via autofluorescence (grey).

In comparison to healthy mice, the glomeruli of NTN treated animals at d14 show a loss of CD31 expression of the glomerular vasculature (CD31, red) indicating the vessel damage. Furthermore the capillary lumen is narrowed and the glomerulus is surrounded by strongly increased fibrous tissue (SHG, blue). Highly autofluorescent spots (grey) in the surrounding tubules might be caused by apoptotic cells while the tissue itself loses its autofluorescence due to tissue damage.

### **Supplementary video 4: qWOB glomeruli quantification**

To demonstrate the identification of all glomeruli in a kidney, the vascular signal (CD31, red) of glomeruli was highlighted in a 3D-reconstruction of a whole-kidney LSFM Z-stack via the "Spots" tool of Imaris. Identified glomeruli are indicated as turquoise balls. For the fully automated quantification of glomeruli in a total of 23 kidneys a self scripted algorithm was used (see methods).